ISSN 1027-4510, Journal of Surface Investigation: X-ray, Synchrotron and Neutron Techniques, 2016, Vol. 10, No. 5, pp. 1077–1086. © Pleiades Publishing, Ltd., 2016.
Original Russian Text © V.I. Shapovalov, A.E. Komlev, V.V. Vit'ko, A.V. Zav'yalov, A.E. Lapshin, S.A. Moshkalev, V.A. Ermakov, 2016, published in Poverkhnost', 2016, No. 10, pp. 88–97.

Influence of Annealing on the Optical Properties and Chemical and Phase Compositions of Tungsten-Oxide Films

V. I. Shapovalov*, A. E. Komlev, V. V. Vit'ko, A. V. Zav'yalov, A. E. Lapshin, S. A. Moshkalev, and V. A. Ermakov

Saint Petersburg Electrotechnical University LETI, St. Petersburg, 197376 Russia

**e-mail: vishapovacov@mail.ru*

Received October 20, 2015

Abstract—The results of investigating the optical properties, chemical composition, and crystal structure of tungsten-oxide films annealed in vacuum and air at 700°C are presented. The films are deposited by means of reactive dc magnetron sputtering. The samples involving single films, as well as heterostructures with tungsten- and titanium-oxide films, located on quartz glass substrates are examined. It is ascertained that, in different samples, annealing leads to different changes in the optical properties, chemical composition, and crystal structure of the films.

Keywords: film, tungsten oxide, reactive dc magnetron sputtering, annealing

DOI: 10.1134/S1027451016040169

INTRODUCTION

In the final quarter of the last century, the increasing application of tungsten oxide (WO_3) films was based on the electrochromic effect arising in the visible wavelength range. For the first time, the results of investigating the electrochromic properties of WO_3 films were reported in [1, 2]. The given issue was discussed in a number of reviews [3–7], where other chromogenic (photo-, gaso-, and thermochromic) properties of WO_3 films were indicated as well. The name of each property indicates an external action, which initiates a change in the optical density of films, leading to their blue coloration. In particular, electrochromic properties stimulate the injection of small-sized ions (H^+, Li^+, and K^+ [5, 8, 9]). Chromogenic properties were employed to create "intelligent" energy-efficient glasses capable of forcibly and autonomously varying transparency under the action of an electric field [10–19] or solar illumination [20], respectively; indicating devices without emission [21]; mirrors with controlled reflection coefficients [4, 22–25], in particular, antiglare mirrors; and the rear-view mirrors of cars [12, 22, 26]. The possibility that WO_3 films can be applied in resistive nonvolatile memory with arbitrary access [27, 28] and optical recording and storage devices (UV photochromic memory) [29] and as optical modulators [30] is now under active study.

In the twenty-first century, interest in WO_3 films appeared due to new prospects. In particular, these films can be employed to produce hydrogen since water undergoes fission on a photoexcited surface [31–49], creating an opportunity for solar-energy accumulation and storage in chemical form. In addition, the application of WO_3 films in the fabrication of solar batteries [50–54] and hydrogen fuel cells [55–59] is being studied.

With the help of the gasochromic properties of films, hydrogen or hydrogen-containing gas sensors are being developed [60–62]. Energy-efficient glasses can be fabricated using photo- and thermochromic effects [3, 63, 64]. Recent results of investigations into the thermochromism of WO_3 films can be found in [65, 66].

Deposited WO_3 films always contain oxygen vacancies. Hence, their chemical formula is more correctly written as WO_{3-x}. The coloration and discoloration processes are related to a chemical reaction whereby interstitial compounds with variable compositions are formed so that embedded particles are located in the voids and tunnels of the film's crystalline structure [67–69]:

$$WO_{3-x} + xM^+ + xe^- \leftrightarrow M_xWO_{3-x}, \qquad (1)$$

where $M^+ = H^+$, Li^+, Na^+, and K^+ and x is the stoichiometric coefficient varying from zero to unity. Owing to the redox reaction

$$W^{6+} + e^- \leftrightarrow W^{5+}, \quad (2)$$

a new suboxide component arises in the film. Reaction (2) describes the appearance of *F*-type color centers (W^{5+} ions) due to electron capture at oxygen vacancies. Protons compensate the generated charge. Fast proton diffusion into the WO_{3-x} film is ensured by the features of its structure. The main structural element of the WO_{3-x} crystal lattice is a WO_6 oxygen octahedron with the W^{6+} ion placed at the center [70]. The vertices of the octahedron are connected to create a spatial grid with end-to-end channels through which protons diffuse without difficulty.

The absorption band observed in the transmission spectra is caused by intervalent electron transport [71] (sometimes, polarons of small radius [72])

$$W_A^{5+} + W_B^{6+} + h\nu \rightarrow W_A^{6+} + W_B^{5+}, \quad (3)$$

where *A* and *B* are closely spaced tungsten ions and $h\nu$ is the photon energy.

Among a large amount of works devoted to studying the chromogenic properties of tungsten-oxide films and published within the last 15 years, there are only a few papers that deal with thermochromism induced by vacuum annealing. Their results are rather dissimilar and cannot unambigously define the chemical composition, crystalline structure, and their influence on the optical properties of the films.

The films deposited via reactive dc magnetron sputtering [73] or in high-frequency systems [74, 75] and with the use of resistive evaporation [76, 77] or an electron beam [78, 79] have no crystalline phases and exhibit low absorption in the visible wavelength range. However, in some cases, the deposited films were colored and their monoclinic crystalline structure was weakly developed. At the same time, tungsten atoms with W^{4+} or W^{5+} states were not detected in these films [76].

Film coloration without the appearance of crystalline phases and their reduction $W^{6+} \rightarrow W^{5+}$ were observed after vacuum annealing at temperatures of 300–350°C [73, 77–79]. A new state W^{4+} was revealed after annealing at 500°C. At times, oxygen losses were not observed in the film. At other times, the composition varied from $WO_{2.9}$ to $WO_{2.6}$ [77–79]. Several authors did not detect changes in the chemical composition of the films and their crystallization if the annealing temperature was less than 600°C [74, 75]. Preliminary investigations made it possible to ascertain that vacuum annealing stimulates film coloration only at temperatures of more than 600°C, but films include different crystalline phases depending on heat-treatment technology [66, 80, 81].

This work focuses on studying the influence of annealing in vacuum and air on the optical properties, chemical composition, and crystalline structure of one- and two-layer samples containing amorphous TiO_{2-x} and WO_{3-x} films synthsized on quartz glass substrates by means of reactive dc magnetron sputtering.

EXPERIMENTAL

The films were synthesized in a vacuum chamber with a volume of 8×10^{-3} m^3, which was equipped with two planar magnetrons whose metal targets 60 mm in diameter were manufactured from titanium and tungsten. When the partial pressure of argon was 6 mTorr, the O_2 volume flow rate was set so as to ensure the oxide mode of target operation [82] at a discharge-current density of 0.02 A/cm^2. The TiO_{2-x} film growth rate was about 1.8 nm/min if the discharge voltage was 400 V. In the case of WO_{3-x} films, the parameters were 65 nm/min and 690 V, respectively. Experiments were carried out using three types of samples: WO_{3-x}/SiO_2, $WO_{3-x}/TiO_{2-x}/SiO_2$, and $TiO_{2-x}/WO_{3-x}/SiO_2$. Each film was 100–110 nm thick. Below, these samples are designated *A*, *B*, and *C*.

A portion of samples of each type was isothermally annealed in vacuum for 1 h. In this case, the residual pressure was no more than 5×10^{-2} mTorr and the temperature was 700°C. The other portion was treated in air at 700°C. The optical properties and chemical and phase compositions of each sample were studied. The temperature conditions of annealing were chosen from preliminary studies indicating that the properties of the films are considerably affected by vacuum annealing at a temperature of more than 600°C [81].

The spectral transmission coefficients (hereinafter referred to as transmission spectra) were measured in the range of 200–1000 nm with the help of an ISM3600 spectrometer developed at the Saint Petersburg Electrotechnical University LETI. Its resolution was no more than 2.0 nm, and the absolute error of measurement of the wavelengths was no more than ±0.5 nm. An optical signal was supplied to a measuring device through a quartz monofilament 0.4 mm in diameter. In the regions of 400–900 and 200–400 nm, measurements were performed using a halogen light source and LD2(D) deuterium lamp, respectively.

The chemical composition of the films was investigated by means of the Raman scattering method. The Raman scattering spectra were recorded in the backscattering geometry at room temperature. The recording procedure was performed using an NT–MDT (Russia) Ntegra Spectra confocal spectrometer. The excitation source was a laser with an emission wavelength of 473 nm. The laser beam was focused into a spot 1–2 μm in diameter on the sample surface. To avoid any effect of the laser on the objects under study,

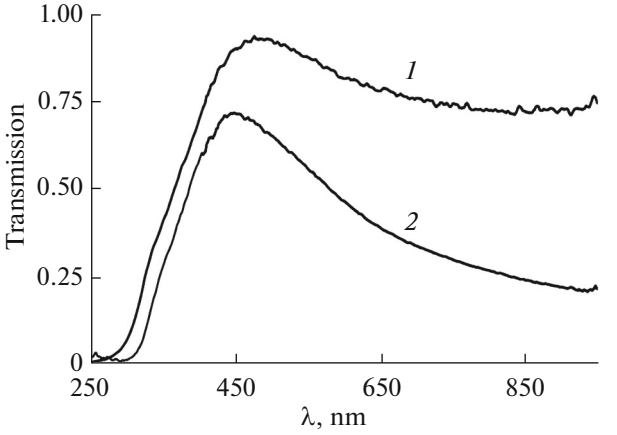

Fig. 1. Transmission spectra of samples *A* after (*1*) synthesis and (*2*) vacuum treatment.

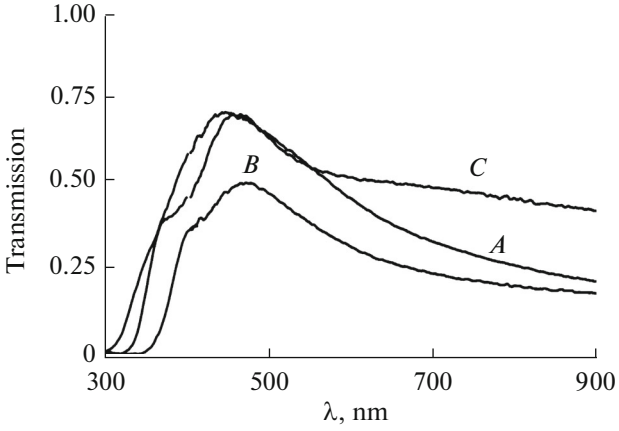

Fig. 2. Transmission spectra of the samples annealed in vacuum.

the emission power density was set to not exceed 10 kW/cm^2.

The films were examined via X-ray phase analysis (XRPA) with the help of a Bruker D8 Advance powder X-ray diffractometer with CuK_α radiation (the operating voltage is 40 kV at a current of 40 mA). Phase analysis was carried out with the use of the ICDD-2006 international database. The average size of crystallites determined by means of the Scherrer method with allowance for instrumental broadening of the peak profiles and the ratio of phases were calculated using the TOPAS software package included in the diffractometer software.

RESULTS AND DISCUSSION

Heat Treatment in Vacuum

After annealing, the transmission spectrum of sample *A* underwent substantial changes (Fig. 1). A wide absorption band with a peak in the near IR range (900–920 nm) appeared in it. As a consequence, the film became colored blue. Analogous results were obtained for samples *B* and *C* (Fig. 2).

In [83], it was found that the transmission spectra of TiO_{2-x}/SiO_2 samples do not undergo considerable changes upon heat treatment in vacuum. Hence, the revealed thermochromism should be attributed exclusively to the properties of WO_{3-x} films.

The fact that *F*-type color centers are generated due to vacuum heating can be explained as follows. The synthesized highly porous WO_{3-x} film contains adsorbed water. At a sufficiently high temperature, sample treatment leads to evaporation, the partial dissociation of H_2O molecules, and the ionization of atomic hydrogen on the film surface. The proton H^+ and electron e^- diffuse into the film. Due to the given process which satisfies reaction (1), hydrogen-tungsten bronze (HTB) is formed:

$$WO_{3-x} + xH^+ + xe^- \leftrightarrow H_xWO_{3-x}. \quad (4)$$

When the film is heated in vacuum, the concentration of *F*-type centers increases because oxygen leaves the surface layer [45, 46]. Therefore, it can be supposed that intervalent electron transport (3) excites absorption in the near IR range observed in the spectra of Fig. 2.

Table 1. Consolidated results of the vacuum thermal treatment of samples

No.	Sample	Tetragonal TiO_2 phase (sp. gr. $P4_2/mnm$)				Cubic H_xWO_3 phase (sp. gr. $Pm\bar{3}m$)			*R*, %
		a, Å	*c*, Å	*d*, nm	*D*, %	*a*, Å	*d*, nm	*D*, %	
1	*A*	–				3.76	27	100	5.3
2	*B*	3.81	9.43	100	40	3.79	15	60	5.2
3	*C*	3.81	9.47	250	30	3.76	25	70	4.9

Here, *a* and *c* are the cell parameter, *d* is the crystallite size, *D* is the phase fraction in the film, and *R* is the uncertainty parameter.

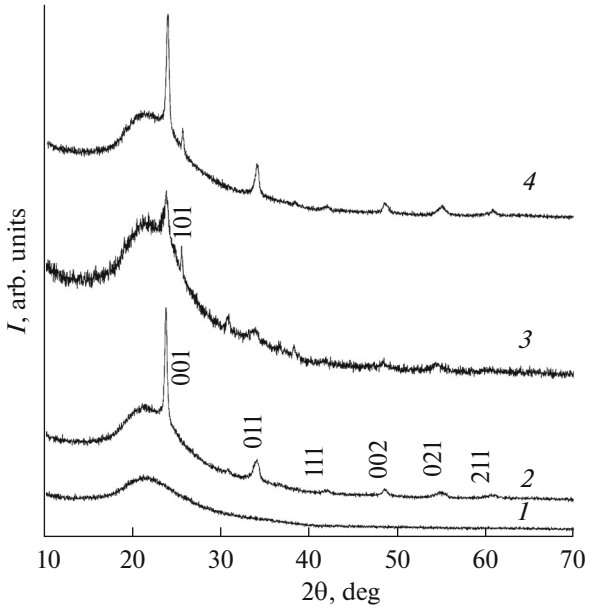

Fig. 3. X-ray diffraction patterns of the samples after (*1*) deposition and annealing: (*2*) sample *A*, cubic phase, (*3*) sample *B* (101 peak corresponds to the anatase phase of TiO_2), and (*4*) sample *C*.

To obtain detailed information on the detected effects, let us consider the XRPA results presented in Table 1 and Fig. 3. The synthesized films of all samples were X-ray amorphous (Fig. 3, curve *1*). After vacuum annealing, the cubic HTB phase (H_xWO_3) was generated in the amorphous matrix (Fig. 3, curve *2*; Table 1, row 1).

Table 2. Band positions (cm^{-1}) in the Raman scattering spectra of the films corresponding to vacuum-annealed samples

Sample			Mode	Reference
A	*B*	*C*		
233	239	–	$O–W^{4+}–O$	[84]
–	–	273	O–W–O	[85]
384	350	336	$W^{5+}–O$	[86]
–	–	393	$AB_{1g}(1)$	[87]
436	434	–	$W^{5+}=O$	[85]
–	–	513	AA_{1g}	[87]
–	–	636	AB_{1g}	[87]
689	674	657	O–W–O	[88]
–	–	721	W–O	[89]
788	763	798	$W^{6+}–O$	[71]
–	–	809	W–O	[89]
913	831	889	O–W–O	[88]

Owing to the similar heat treatment of samples *B* and *C*, crystalline HTB phases and, additionally, a TiO_2 anatase phase appeared in them (Fig. 3, 4, curves 3; Table 1, rows 2, 3). When TiO_{2-x}/SiO_2 samples are heat treated in vacuum, the crystalline phase of TiO_2 does not develop in such samples. Hence, the opposite result for the titanium-oxide film in heterostructures can be associated with interference between crystallization processes in the layers. However, results vary upon passing from one heterostructure to another.

Thus, the XRPA data confirm the assumption made above: a change in the optical properties of the samples under study, which is detected after heat treatment in vacuum, is related to HTB formation in the WO_3 film.

After deposition, the Raman scattering spectra of samples *A* (Fig. 4a) incorporate two relatively wide asymmetric bands in the regions of 200–400 and 600–1100 cm^{-1}. Deconvolution of the spectra made it possible to reveal five bands which relate to films with stoichiometric compositions and peaks corresponding to the following shifts: 274, 329, and 686 cm^{-1} which are typical of the vibration modes of the O–W–O bridge bond; 800 cm^{-1} which characterizes $W^{6+}–O$ bond oscillations in the WO_6 octahedron; and 963 cm^{-1} belonging to the vibration mode under the stretching of end oxygen atoms $W^{6+} = O$ (probably, on the WO_3 cluster surface or in film micropores). The last band is evidence that an amorphous phase exists in the film.

In samples *A*, the Raman scattering spectra of films colored due to annealing contain up to eight bands (Fig. 4b; Table 2). The band corresponding to 983 cm^{-1} disappeared. Instead, a band characterizing the stretching of end oxygen atoms $W^{5+} = O$ (at a shift of 436 cm^{-1}) is observed. The latter indicates that the films were incompletely crystalized. Moreover, the spectra have bands whose peaks correspond to 233 cm^{-1} (conceivably, this position belongs to the oscillatory mode of the $O–W^{4+}–O$ bridge bond) and 384 cm^{-1} typical of $W^{5+}–O$ bond oscillations in the WO_6 octahedron.

The results discussed above indicate that the reduction of two types of tungsten atoms occurs in WO_{3-x} films during heat treatment in vacuum:

$$W^{6+} + e^- \leftrightarrow W^{5+} \text{ and } W^{5+} + e^- \leftrightarrow W^{4+}.$$

Therefore, intervalent transport (3) can be supplemented by two coloration mechanisms:

$$W_A^{5+} + W_B^{4+} + h\nu \rightarrow W_A^{4+} + W_B^{5+}, \quad (5)$$

$$W_A^{6+} + W_B^{4+} + h\nu \rightarrow W_A^{4+} + W_B^{6+}. \quad (6)$$

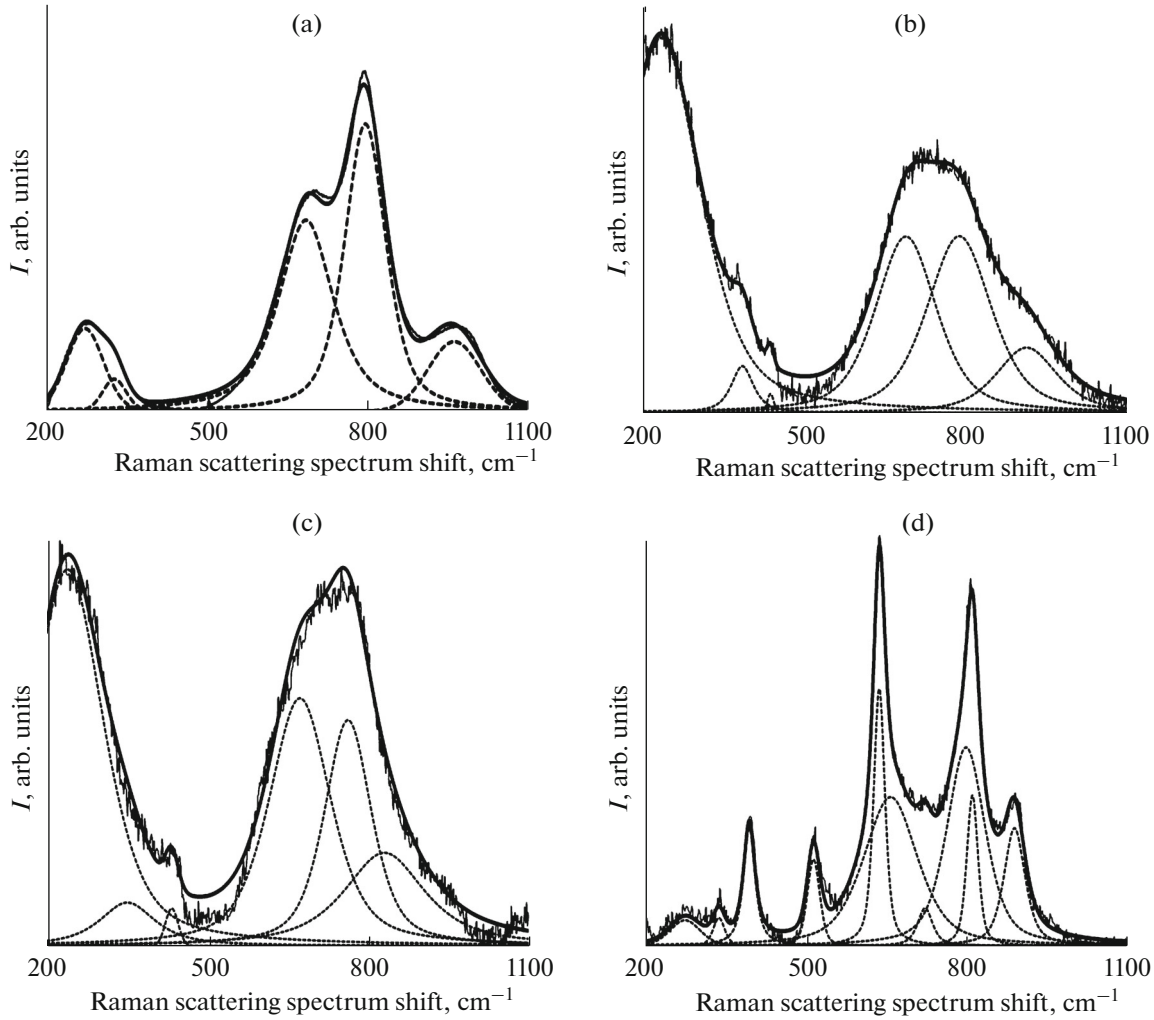

Fig. 4. Raman scattering spectra of the samples: (a) sample *A* after deposition and (b–d) samples *A*, *B*, and *C* after vacuum annealing, respectively. The experiment corresponds to a thin continuous line, spectral components are shown by dotted lines, and the sum is designated by a thick continuous line.

The spectrum of samples *B* resembles those of samples *A* (Fig. 4c; Table 2). Although the TiO_{2-x} film is included in samples *B*, their spectra do not contain the corresponding bands in spite of the fact that, as is evident from the XRPA data, the amount of the hexagonal crystalline phase of TiO_2 (sp. gr. $P4_2/mnm$) is 40% and the cubic phase (sp. gr. $Pm\bar{3}m$) of $H_{0.5}WO_3$ HTB occupies about 60% (Table 1).

It seems that the reason for the aforementioned situation is as follows. Approximately 50% of the emission of the laser used in the spectrometer (its wavelength is 473 nm) is absorbed in the colored WO_{3-x} film of sample *B* (Fig. 2). Hence, a weaker signal excites Raman scattering. The signal of the lower TiO_{2-x} film is absorbed and, in part, diffusely scattered in the crystalline phase of the upper WO_{3-x} film.

The spectra of samples *C* differ appreciably from two previous variants (Fig. 4d; Table 2), demonstrating that only tungsten atom reduction (2) arose in the WO_{3-x} films. Hence, their coloration is described by mechanism (3). Indeed, in these samples, the observed color of the WO_{3-x} films is less intense, and their transmission spectra in the near IR range are at a level of 45%. At the same time, for two other samples, this quantity is less than 25% (Fig. 2).

Annealing in Air

On account of the given type of annealing, the spectral transmission coefficient decreased uniformly in the visible wavelength range of all samples (Fig. 5). This is commonly related to the fact that radiation is diffusely scattered at the crystalline phase. Hence, the observed changes in the spectra (Fig. 5) serve as indi-

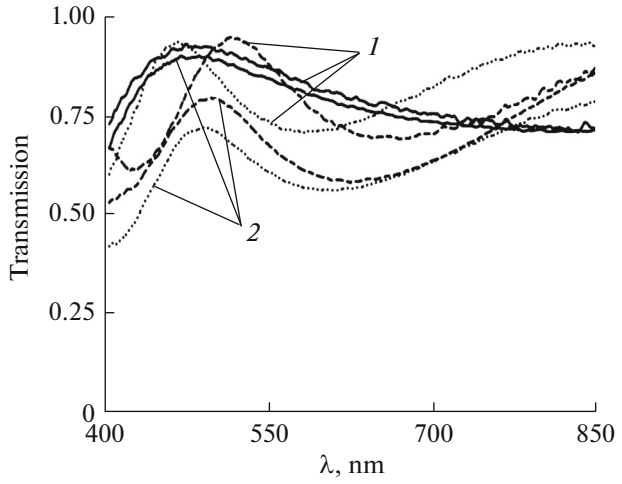

Fig. 5. Transmission spectra of samples *A* (continuous lines), *B* (dashed lines), and *C* (dotted lines) after (*1*) synthesis and (*2*) vacuum treatment.

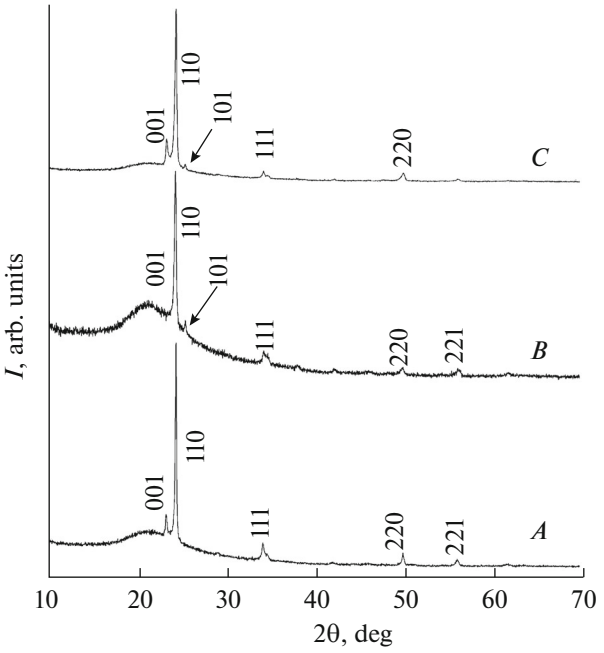

Fig. 6. X-ray diffraction patterns of samples *A*, *B*, and *C* annealed in air. The (101) peaks corresponding to the anatase phase of TiO_2 are shown by arrows in the diffraction patterns of samples *B* and *C*.

rect evidence of amorphous-film crystallization, as was confirmed by the XRPA results.

As a consequence of heat treatment, the tetragonal WO_3 phase (Fig. 6) was formed in all samples. Its most intense peak corresponding to the (110) plane is observed at $2\theta = 24.34°$. The 001 and 110 peaks were superimposed on each other (Fig. 6, curves *3*; $2\theta \sim 23.4°$) in the diffraction patterns of samples *B*. The corrected parameters of the unit cell of the tetragonal phase (sp. gr. *P*4/*nmm*), which are presented in Table 3 for all samples, correspond to a titanium-oxide film of stoichiometric composition. The composition and crystalline structure of the WO_3 film of sample *C* are similar to those of sample *A*. This implies that, in samples *A* and *C*, WO_3 films are generated under identical conditions. At the same time, in the former and latter cases, the source of oxygen of the WO_3 film is a gas medium and TiO_2 film, respectively.

After heat treatment in air at 700°C, it was revealed [83] that the anatase phase with unit-cell parameters inherent to the TiO_2 stoichiometric composition develops in TiO_{2-x}/SiO_2 samples. For titanium oxide in samples *C*, the result is somewhat different. This can be explained by the fact the crystallization process occurring in the lower WO_{3-x} layer affects the development of the crystalline phase in the upper TiO_{2-x} layer.

An analogous reason can underlie the discrepancy between the parameters *c* of unit cells in samples *A* and *B* (Table 3, rows 1 and 2) and the superimposition of the 001 and 110 peaks in the diffraction patterns of samples *B*. However, in the given case, the crystallization process observed in the lower TiO_{2-x} layer affects the development of the crystalline phase in the upper WO_{3-x} layer.

In the Raman scattering spectra (Fig. 7a), there are four relatively wide asymmetric bands in the regions of 200–400 and 500–1000 cm^{-1}. The deconvolution of

Table 3. Consolidated XRPA results obtained after sample annealing in air

No.	Sample	Tetragonal TiO_2 phase (sp. gr. $P4_2/mnm$)				Tetragonal WO_3 phase (sp. gr. *P*4/*nmm*)				*R*, %
		a, Å	*c*, Å	*d*, nm	*D*, %	*a*, Å	*c*, Å	*d*, nm	*D*, %	
1	*A*	–				5.17	3.81	76	100	9.0
2	*B*	3.78	9.46	198	10	5.19	3.75	53	90	5.8
3	*C*	Anatase traces ≤ 1%				5.20	3.84	50	99	8.3

Here, *a* and *c* are the cell parameter, *d* is the crystallite size, *D* is the phase fraction in the film, and *R* is the uncertainty parameter.

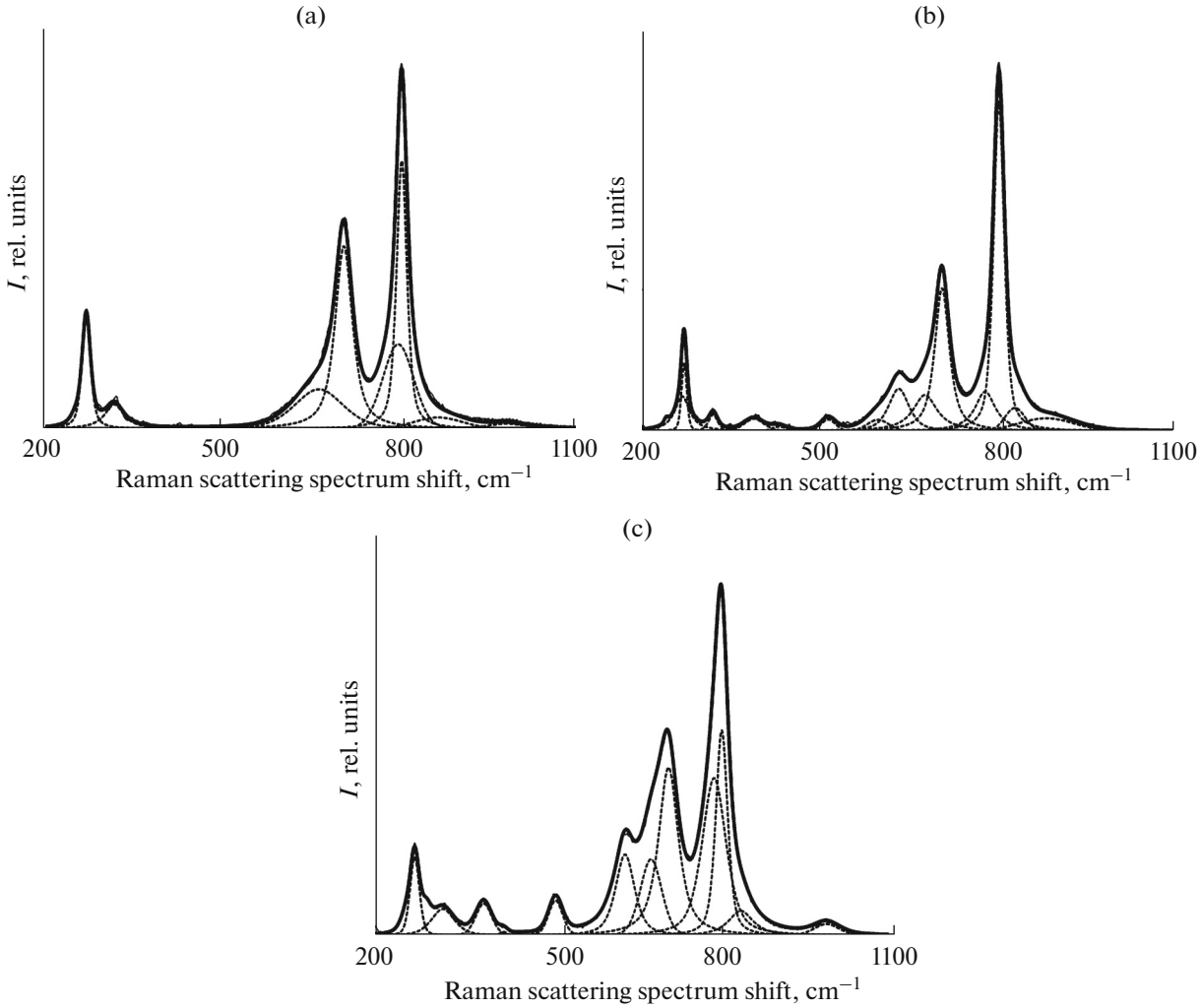

Fig. 7. Raman scattering spectra of the samples: (a–c) samples *A*, *B*, and *C* after annealing in air, respectively. The experiment corresponds to a thin continuous line, spectral components are shown by dotted lines, and the sum is designated by a thick continuous line.

spectra made it possible to detect bands with peak positions presented in Table 4. From the XRPA results (Table 4), it can be assumed that the found bands are inherent to stoichiometric films containing the tetragonal WO_3 phase. The fact that the spectra incorporate a weak band (at a shift of 983 cm^{-1}), which indicates the stretching of end oxygen atoms $W^{5+} = O$, is evidence that the film comprises an amorphous phase.

The above assumption was confirmed by the results of investigations of samples *B* and *C*. In the Raman scattering spectra of the samples whose films are differently arranged on the substrate, the spectral lines have different positions. Analysis demonstrated that the spectrum of sample *B* (Fig. 7b; Table 4) involves two groups of bands with peaks inherent to tungsten-oxide- and titanium-oxide films. In the former case, the peaks correspond to 273, 322, 680, 708, 781, 804, 831, and 884 cm^{-1}. In the latter case, the peaks are observed both at shifts of 424 and 610 cm^{-1} typical of rutile modes and at 393, 515, and 635 cm^{-1} corresponding to anatase modes.

It should be noted that the X-ray diffraction patterns of sample *B* include only peaks of tetragonal crystalline WO_3 ($P4/nmm$) and TiO_2 ($P4_2/mnm$) phases whose ratio is 90 : 10 (Table 3). Rutile was not detected. This indicates that the sensitivity of the Raman-scattering method is higher.

The Raman scattering spectrum of sample *C* includes two groups of bands corresponding to tungsten and titanium oxides. In the former case, the shifts are 273, 336, 680, 710, 790, 802, 836, and 985 cm^{-1}. In the latter case, the shifts are 424 and 610 cm^{-1}, which are inherent to rutile modes, and 393, 515, and 635 cm^{-1}, which are characteristic of anatase modes.

Table 4. Band positions (cm^{-1}) in the Raman scattering spectra of the films corresponding to air-annealed samples

Sample			Mode	Reference
A	*B*	*C*		
–	242	–	R–O–O	[84]
270	273	273	O–W–O	[85]
318	322	336	O–W–O	[90]
–	391	393	$AB_{1g}(1)$	[86]
–	432	424	RE_g	[91]
–	516	515	AA_{1g}	[91]
–	600	610	RA_{1g}	[91]
–	635	635	AB_{1g}	[91]
665	680	680	O–W–O	[88]
707	708	710	W–O	[89]
799	781	790	W^{6+}–O	[71]
805	804	802	W–O	[89]
867	831	836	O–W–O	[88]
983	884	985	W^{6+}=O	[88]

CONCLUSIONS

The performed X-ray diffraction and spectral studies of the WO_3/SiO_2, $TiO_2/WO_3/SiO_2$ and $WO_3/TiO_2/SiO_2$ samples have made it possible to reveal that, after vacuum annealing at a temperature of 700°C, a wide absorption band with a peak located in the near-infrared range arises in the transmission spectra of these samples. As a result, the film becomes colored blue.

In the WO_3/SiO_2 and $WO_3/TiO_2/SiO_2$ samples, thermochromism is caused by tungsten-ion reduction in the lattice, namely, $W^{6+} + e^- \leftrightarrow W^{5+}$ and $W^{5+} + e^- \leftrightarrow W^{4+}$. In the $TiO_2/WO_3/SiO_2$ samples, thermochromism appears due to the reduction $W^{6+} + e^- \leftrightarrow W^{5+}$ and is related to the fact that the cubic phase of $H_{0.5}WO_3$ hydrogen-tungsten bronze is formed in the amorphous matrix of tungsten-oxide films.

Due to annealing in air, stoichiometric films containing a tetragonal WO_3 phase are generated in the WO_3/SiO_2 samples. Crystalline phases differing from those identified in the corresponding samples with single films are created in the upper films of $WO_3/TiO_2/SiO_2$ and $TiO_2/WO_3/SiO_2$ samples.

ACKNOWLEDGMENTS

This study was supported by the Russian National Foundation, project no. 15-19-00076.

REFERENCES

1. S. K. Deb, Appl. Opt. **8**, 192 (1969).
2. S. K. Deb, Philos. Mag. **27**, 801 (1973).
3. S. K. Deb, Sol. Energy Mater. Sol. Cells **92**, 245 (2008).
4. C. G. Granqvist, E. Avendano, and A. Azens, Thin Solid Films **442**, 201 (2003).
5. A. L. Gusev, T. N. Kondyrina, V. V. Kursheva, I. A. Pishchurova, O. N. Efimov, S. A. Kondrashov, and A. V. Vannikov, Al'tern. Energ. Ekol., No. 10, 122 (2009).
6. C. G. Granqvist, P. C. Lansaker, N. R. Mlyuka, G. A. Niklasson, and E. Avendano, Sol. Energy Mater. Sol. Cells **93**, 2032 (2009).
7. C. G. Granqvist, Sol. Energy Mater. Sol. Cells **60**, 201 (2000).
8. O. V. Anisimov, V. I. Gaman, N. K. Maksimova, Yu. P. Naiden, V. A. Novikov, E. Yu. Sevast'yanov, F. V. Rudov, and E. V. Chernikov, Semiconductors **44** (3), 366 (2010).
9. C.-C. Liao, Sol. Energy Mater. Sol. Cells **99**, 26 (2012).
10. H. N. Cui, M. F. Costa, V. Teixeira, I. Porqueras, and E. Bertran, Surf. Sci. **532–535**, 1127 (2003).
11. A. Karuppasamy and A. Subrahmanyam, Thin Solid Films **516**, 175 (2007).
12. A. Karuppasamy and A. Subrahmanyam, J. Appl. Phys. **101**, 113522 (2007).
13. L. J. Berggren, C. Jonsson, and G. A. Niklasson, J. Appl. Phys. **102**, 083538 (2007).
14. C.-Y. Kim, S.-G. Cho, and T.-Y. Lim, Sol. Energy Mater. Sol. Cells **93**, 2056 (2009).
15. A. Subrahmanyam, C. S. Kumar, and K. M. Karuppasamy, Sol. Energy Mater. Sol. Cells **91**, 62 (2007).
16. J.-L. Chiang, S.-S. Jan, J.-C. Chou, and Y.-C. Chen, Sens. Actuators, B **76**, 624 (2011).
17. R.-H. Ma and Y.-C. Chen, Sensors **12**, 359 (2012).
18. S. H. N. Lim, J. Isidorsson, L. Sun, B. L. Kwak, and A. Anders, Sol. Energy Mater. Sol. Cells **108**, 129 (2013).
19. G. Leftheriotis, G. Syrrokostas, and P. Yianoulis, Sol. Energy Mater. Sol. Cells **94**, 2304 (2010).
20. S. N. Alamri, Sol. Energy Mater. Sol. Cells **93**, 1657 (2009).
21. M. Vasilopoulou, A. Botsialas, P. Argitis, G. Aspiotis, G. Papadimitropoulos, and D. Davazoglou, Phys. Status Solidi C **5**, 3868 (2008).
22. K. Tajima, Y. Yamada, S. Bao, M. Okada, and K. Yoshimura, Surf. Coat. Technol. **202**, 5633 (2008).
23. K. Tajima, Y. Yamada, S. Bao, M. Okada, and K. Yoshimura, Solid State Ionics **180**, 654 (2009).
24. K. Tajima, H. Hotta, Y. Yamada, M. Okada, and K. Yoshimura, Appl. Phys. Lett. **101**, 251907 (2012).
25. K. Tajima, Y. Yamada, S. Bao, M. Okada, and K. Yoshimura, Sol. Energy Mater. Sol. Cells **92**, 120 (2008).
26. M. Al-Kuhaili, A. Al-Aswad, S. Durrani, and I. Bakhtiari, Sol. Energy **86**, 3183 (2012).
27. D. S. Shang, L. Shi, J. R. Sun, B. G. Shen, F. Zhuge, R. W. Li, and Y. G. Zhao, Appl. Phys. Lett. **96**, 072103 (2010).

28. D. S. Shang, L. Shi, J.-R. Sun, and B.-G. Shen, J. Appl. Phys. **111**, 053504 (2012).
29. Y. Zhang, S.-H. Lee, A. Mascarenhas, and S. K. Deb, Appl. Phys. Lett. **93**, 203508 (2008).
30. A. A. Joraid, Appl. Phys. **9**, 73 (2009).
31. J. H. Park, O. O. Park, and S. Kim, Appl. Phys. Lett. **89**, 163106 (2006).
32. S. Cwik, A. P. Milanov, V. Gwildies, T. B. Thiede, V. S. Vidyarthi, A. Savan, R. Meyer, H. W. Becker, D. Rogalla, A. Ludwig, R. A. Fischer, et al., ECS Trans. **28**, 159 (2010).
33. Y. A. Shaban and S. U. M. Khan, Int. J. Photoenergy, **749135** (2012), . doi 10.1155/2012/749135
34. S. Biswas and J. Baeg, Int. J. Hydrogen Energy **38**, 317 (2013).
35. Á. Valdés and G. Kroes, J. Chem. Phys. **130**, 114701 (2009).
36. C. Lai and S. Sreekantan, Mater. Sci. Semicond. Process. **16**, 303 (2013).
37. S. K. Biswas, J.-O. Baeg, S.-J. Moon, K.-J. Kong, and W.-W. So, J. Nanopart. Res. **14**, 1 (2012).
38. D.-S. Lee, K.-H. Nam, and D.-D. Lee, Thin Solid Films **375**, 142 (2000).
39. A. Mao, J. K. Kim, K. Shin, D. H. Wang, P. J. Yoo, G. Y. Han, and J. H. Park, J. Power Sources **210**, 32 (2012).
40. S. J. Hong, H. Jun, and J. S. Lee, Scr. Mater. **63**, 757 (2010).
41. W. J. Lee, P. S. Shinde, G. H. Go, and E. Ramasamy, Int. J. Hydrogen Energy **36**, 5262 (2011).
42. P. S. Shinde, G. G. Go, and W. J. Lee, Int. J. Energy Res. **37**, 323 (2013).
43. L. Meda, G. Tozzola, A. Tacca, G. Marra, S. Caramori, V. Cristino, and C. A. Bignozzi, Sol. Energy Mater. Sol. Cells **94**, 788 (2010).
44. A. I. Gavrilyuk, Sol. Energy Mater. Sol. Cells **94**, 515 (2010).
45. A. Memar, W. R. W. Daud, S. Hosseini, E. Eftekhari, and L. J. Minggu, Sol. Energy **84**, 1538 (2010).
46. K. Miecznikowski, P. J. Kulesza, and S. Fiechter, Appl. Surf. Sci. **257**, 8215 (2011).
47. J. W. J. Hamilton, J. A. Byrne, P. S. M. Dunlop, and N. M. D. Brown, Int. J. Photoenergy, **185479** (2008), doi 10.1155/2008/185479
48. K. Sivula, F. L. Formal, and M. Grätzel, Chem. Mater. **21**, 2862 (2009).
49. S. J. Hong, H. Jun, P. H. Borse, and J. S. Lee, Int. J. Hydrogen Energy **34**, 3234 (2009).
50. L. Fang, S. J. Baik, K. S. Lim, S. H. Yoo, M. S. Seo, S. J. Kang, and J. W. Seo, Appl. Phys. Lett. **96**, 193501 (2010).
51. C. Tao, S. Ruan, G. Xie, X. Kong, L. Shen, F. Meng, C. Liu, X. Zhang, W. Dong, and W. Chen, Appl. Phys. Lett. **94**, 043311 (2009).
52. Y. Saito, S. Uchida, T. Kubo, and H. Segawa, Thin Solid Films **518**, 3033 (2010).
53. A. Z. Sadek, H. Zheng, M. Breedon, V. Bansal, S. K. Bhargava, K. Latham, J. Zhu, L. Yu, Z. Hu, P. G. Spizzirri, W. Wlodarski, et al., Langmuir **25**, 9545 (2009).
54. P. Cheng, C. S. Deng, D. N. Liu, and X. M. Dai, Appl. Surf. Sci. **254**, 3391 (2008).
55. K.-W. Park, K.-S. Ahn, J.-H. Choi, Y.-C. Nah, Y.-M. Kim, and Y.-E. Sung, Appl. Phys. Lett. **81**, 907 (2002).
56. J. Zhao, A. V. Knotko, L. A. Frolova, and Yu. A. Dobrovolsky, Al'tern. Energ. Ekol., No. 8, 175 (2009).
57. B. Wickman, M. Wesselmark, C. Lagergren, and G. Lindbergh, Electrochim. Acta **56**, 9496 (2011).
58. M. Wesselmark, B. Wickman, C. Lagergren, and G. Lindbergh, Electrochim. Acta **55**, 7590 (2010).
59. S. Suzuki, T. Onodera, J. Kawaji, T. Mizukami, and K. Yamaga, Appl. Catal., A **427–428**, 92 (2012).
60. C.-H. Hsu, C.-C. Chang, K.-W. Yeh, Y.-R. Wu, C.-C. Chan, M.-J. Wang, M.-K. Wu, Thin Solid Films **520**, 1470 (2011).
61. T. Watanabe, S. Okazaki, H. Nakagawa, K. Murata, K. Fukuda, Sens. Actuators, B **145**, 781 (2010).
62. M. Ranjbar, N. T. Garavand, S. M. Mahdavi, and A. Irajizad, Sol. Energy Mater. Sol. Cells **94**, 201 (2010).
63. S. Songara, V. Gupta, M. K. Patra, J. Singh, L. Saini, G. S. Gowd, S. R. Vadera., and N. Kuma, J. Phys. Chem. Solids **73**, 851 (2012).
64. T. Hagizawa, T. Honma, Y. Kuroki, T. Okamoto, and M. Takata, Ceram. Int. **39**, 2851 (2013).
65. G. Leftheriotis, S. Papaefthimiou, P. Yianoulisa, and A. Siokoub, Thin Solid Films **384**, 298 (2001).
66. V. I. Shapovalov, A. E. Lapshin, A. E. Komlev, and A. A. Komlev, Techn. Phys. Lett. **38** (6), 555 (2012).
67. S. J. Yoo, Y. H. Jung, J. W. Lim, H. G. Choi, D. K. Kim, and Y.-E. Sung, Sol. Energy Mater. Sol. Cells **92**, 179 (2008).
68. S. R. Bathe and P. S. Patil, Solid State Ionics **179**, 314 (2008).
69. G. Abadías, A. S. Gago, and N. Alonso-Vante, Surf. Coat. Technol. **205**, 265 (2011).
70. E. Broclawik, A. Góra, P. Liguzinski, P. Petelenz, and H. A. Witek, J. Chem. Phys. **124**, 054709 (2006).
71. E. Ozkan, S.-H. Lee, C. E. Tracy, and J. R. Pitts, Sol. Energy Mater. Sol. Cells **79**, 439 (2003).
72. A. I. Inamdar, Y. S. Kim, B. Jang, H. Im, W. Jung, D.-Y. Kim, and H. Kim, Thin Solid Films **520**, 5367 (2012).
73. A. Romanyuk and P. Oelhafen, Sol. Energy Mater. Sol. Cells **90**, 1945 (2006).
74. T. G. G. Maffeis, D. Yung, L. LePennec, M. W. Penny, R. J. Cobley, E. Comini, G. Sberveglieri, and S. P. Wilks, Surf. Sci. **601**, 4953 (2007).
75. T. G. G. Maffeis, M. W. Penny, R. J. Cobley, E. Comini, G. Sberveglieri, and S. P. Wilks, J. Surf. Sci. Nanotech. **7**, 319 (2009).
76. A. H. Jayatissa, S.-T. Cheng, and T. Gupta, Mater. Sci. Eng., B **109**, 269 (2004).
77. S. M. A. Durrani, E. E. Khawaja, M. A. Salim, M. F. Al-Kuhaili, and A. M. Al-Shukri, Sol. Energy Mater. Sol. Cells **71**, 313 (2002).
78. A. Siokou, G. Leftheriotis, S. Papaefthimiou, and P. Yianoulis, Surf. Sci. **482–485**, 294 (2001).

79. G. Leftheriotis, S. Papaefthimiou, P. Yianoulisa, and A. Siokou, Thin Solid Films **384**, 298 (2001).
80. V. I. Shapovalov, A. E. Lapshin, A. E. Komlev, M. U. Arsent'ev, and A. A. Komlev, Tech. Phys. **58** (9), 1313 (2013).
81. A. E. Lapshin, V. I. Shapovalov, A. E. Komlev, M. Yu. Arsent'ev, A. A. Komlev, Glass Phys. Chem. **39** (5), 563 (2013).
82. A. A. Barybin and V. I. Shapovalov, J. Appl. Phys. **101**, 054905 (2007).
83. A. E. Komlev, A. E. Lapshin, O. V. Magdysyuk, V. V. Plotnikov, V. I. Shapovalov, and N. S. Shutova, Techn. Phys. Lett. **36** (10), 942 (2010).
84. K. M. Karuppasamy and A. Subrahmanyam, J. Phys. D: Appl. Phys. **42**, 095301 (2009).
85. A. Cremonesi, Y. Djaoued, D. Bersani, and P. P. Lottici, Thin Solid Films **516**, 4128 (2008).
86. S.-H. Lee, H. M. Cheong, P. Liu, D. Smith, C. E. Tracy, A. Mascarenhas, J. R. Pitts, and S. K. Deb, Electrochim. Acta **46**, 1995 (2001).
87. U. Balachandran and N. G. Eror, J. Solid State Chem. **42**, 276 (1982).
88. E. B. Santos, J. M. S. Silva, F. A. Sigoli, and I. O. Mazali, J. Nanopart. Res. **13**, 5909 (2011).
89. C. V. Ramana, S. Utsunomiya, R. C. Ewing, C. M. Julien, and U. Becker, J. Phys. Chem. B **110**, 10430 (2006).
90. E. Ozkan, S.-H. Lee, C. E. Tracy, and J. R. Pitts, Sol. Energy Mater. Sol. Cells **79**, 439 (2003).
91. A. D. Barros, K. F. Albertin, J. Miyoshi, I. Doi, and J. A. Diniz, Microelectron. Eng. **87**, 443 (2010).

Translated by S. Rodikov